JACS
JOURNAL OF THE AMERICAN CHEMICAL SOCIETY

Article

pubs.acs.org/JACS

Ultrathin 2D Coordination Polymer Nanosheets by Surfactant-Mediated Synthesis

Sebastian C. Junggeburth,[‡,⊥] Leo Diehl,[⊥] Stephan Werner,[‡,⊥] Viola Duppel,[‡,⊥] Wilfried Sigle,[§] and Bettina V. Lotsch*[,‡,⊥]

[‡]Max Planck Institute for Solid State Research Stuttgart, Heisenbergstraße 1, 70569 Stuttgart, Germany

[§]Max Planck Institute for Intelligent Systems, Stuttgart Centre for Electron Microscopy, Heisenbergstraße 3, 70569 Stuttgart, Germany

[⊥]Department of Chemistry and Center for Nanoscience (CeNS), Ludwig-Maximilians-Universität, Butenandtstraße 5-13, 81377 München, Germany

Supporting Information

ABSTRACT: Low-dimensional nanostructures offer a host of intriguing properties which are distinct from those of the bulk material, owing to size-confinement effects and amplified surface areas. Here, we report on the scalable, bottom-up synthesis of ultrathin coordination polymer nanosheets via surfactant-mediated synthesis and subsequent exfoliation. Layers of a two-dimensional (2D) zinc coordination polymer are self-assembled in the interlamellar space of a reverse microemulsion mesophase into stacks of nanosheets interleaved with cethyltrimethylammonium bromide (CTAB) at regular intervals, thus giving rise to a lamellar hybrid mesostructure with a lattice period of ~8 nm and an underlying highly crystalline substructure. The basic structural motif is composed of 2D acetato–benzimidazolato–zinc layers of tetrahedrally coordinated zinc joined together by anionic acetate and benzimidazolate ligands. The hierarchical structure was studied by PXRD, TEM, EDX, EELS, AFM, and solid-state NMR spectroscopy, revealing a high level of order on both the atomic and mesoscale, suggesting fairly strong interactions along the organic–inorganic hybrid interface. Exfoliation of the hybrid material in organic solvents such as THF and chloroform yields sheet- and belt-like nanostructures with lateral sizes between 10's and 100's of nanometers and a height of about 10 nm measured by AFM, which precisely maps the basal spacing of the lamellar mesostructure; further exfoliation results in nanobelts with minimum sizes around 4 nm. Finally, the sheetlike nanostructures behave as morphological chameleons, transforming into highly regular multiwalled coordination polymer nanotubes upon treatment with organic solvents.

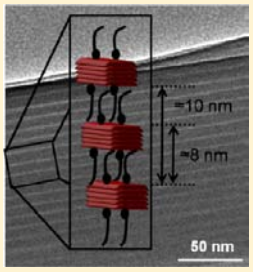

INTRODUCTION

It is commonly accepted in nanoscience that the physical properties depend on the size of the nanomaterial.[1] Therefore, methods for controlling the size distribution of nanomaterials are key prerequisites to gain access to a plethora of interesting properties and size-dependent phenomena inherent to nanomaterials. While bottom-up synthesis methods are highly versatile and allow for a broad range of materials to be processed, they often give rise to products with a broad size distribution.[2] In contrast, physical top-down methods to synthesize nanomaterials such as electron beam or nanoimprint lithography offer a high level of size control and accordingly yield higher levels of monodispersity. However, the materials choice is limited for the latter, and fabrication procedures are often elaborate and costly. Integrating bottom-up with top-down techniques within a *chemical* setting involving solution-processing techniques is therefore highly desired. Exfoliation of layered bulk materials into their two-dimensional (2D) constituents can be considered as such a "best of both worlds" approach, as it combines the versatility of "bottom-up" solid-state synthesis with the high-precision formation of essentially monodisperse nanostructures by "top-down" delamination of preformed nanosheet building blocks. Nevertheless, control over the monodispersity is not always straightforward. Strong interlayer forces within the bulk material and insufficient control of the kinetics of exfoliation tend to break up the solid irregularly into nanosheets with different thicknesses and lateral dimensions. To alleviate such shortcomings, the template-directed bottom-up—or direct—synthesis of 2D nanosheets has recently entered the stage as a powerful alternative to produce size-controlled nanosheets, which takes advantage of the lamellar mesophase of a surfactant acting as a template for the in situ generation of nanosheets.[3−11] Using this protocol, the layered assemblies can be broken up into individual nanosheets more easily, as the surfactant layers act as predetermined breaking points and stabilizing agents against reagglomeration of the nanosheets at the same time. In addition, and as opposed to multistep intercalation–exfoliation protocols, the direct synthesis of 2D nanomaterials involves a single step and hence can be carried out as one-pot reaction.

Layered materials carry a range of attractive anisotropic properties, including mechanical strength along two dimensions, size- or shape-dependent electronic and optical proper-

Received: December 31, 2012
Published: March 13, 2013

   dx.doi.org/10.1021/ja312567v | J. Am. Chem. Soc. 2013, 135, 6157−6164

ties, and high surface areas.[3] Processing schemes for layered materials are manifold, and their susceptibility to soft chemistry protocols such as surfactant-assisted synthesis, intercalation, ion-exchange, and exfoliation qualifies them for a number of applications ranging from catalysis,[12] adsorption,[13] chemical or biosensing[14] to solid-state nanoreactors,[15] anion/cation exchangers,[16] electrode materials,[17] and molecular sieves.[18] The large family of layered materials amenable to soft chemistry processing includes oxide and nonoxide species such as graphite, layered silicates,[19] titanates,[20] perovskites,[21] chalcogenides,[22,23] and layered double hydroxides (LDHs), many of which have been exfoliated into individual nanosheets by exfoliation involving intercalation and ion-exchange of the pristine layered materials, or simply by mechanical or solvent-mediated exfoliation.[24,25] Although bulk coordination (or "hybrid") polymers (composed of metal ions and organic linkers joined via coordinative bonds) which have an inherent 2D structure are abundant, reports about their exfoliation into 2D nanostructures remain suspiciously scarce. The metal–organic framework MOF-2 and $[Cu_2Br(IN)_2]_n$ (IN = isonicotinato) are the first layered coordination frameworks that have been mechanically exfoliated down to the single-sheet level,[26,27] while other groups used 1D and 2D nanomorphologies of Zn–BDC (BDC = 1,4-benzenedicarboxylate) as platforms for small-molecule detection.[28,29] Cheetham and co-workers recently reported on the exfoliation-mediated synthesis of a range of highly crystalline, dense hybrid framework nanosheets based on dimethylsuccinic acid, which offer a host of interesting magnetic, electronic, and mechanical properties, the latter studied by nano-indentation experiments.[30−36]

In this contribution, we present the direct surfactant-mediated bottom-up synthesis of 2D coordination polymer nanosheets as well as multiwalled nanotubes with a unique level of size control. In the present context, the term coordination polymer refers to a metal–organic substructure composed of metal centers (here Zn^{2+}) coordinated to organic linkers (here benzimidazole and acetate). Moreover, we demonstrate that exfoliation proceeds via a mesostructured hybrid phase featuring hierarchical order on the mesoscale, as well as the atomic scale, mediated by in situ liquid-crystal templating during the formation of a highly crystalline, 2D layered, acetato–benzimidazolato–zinc phase under reverse microemulsion conditions.

RESULTS AND DISCUSSION

Mesostructure Synthesis and Characterization. As reported previously, the reaction of methylimidazole (MeIM) and imidazole (IM) with zinc acetate under reverse microemulsion conditions (cetyltrimethylammonium bromide (CTAB)/*n*-heptane/1-hexanol/water) leads to the formation of mesostructured imidazolate frameworks (MIFs) with a basal spacing of roughly 27 Å, composed of 1D zinc coordination polymers interleaved with CTAB.[37] Surprisingly, switching to benzimidazole (BeIM) as ligand gives rise to a mesostructured material, called BeIM-MIF, with a dramatically enlarged lattice constant of ~84 Å. The observed basal spacing does not correspond to typical lamellar mesostructures containing single-layer (26 Å) or bilayer (52 Å) arrangements of CTAB.[37−43] Besides a series of low-angle reflections associated with the mesostructure, the XRD of the white product additionally shows a number of high-angle reflections, indicative of a hierarchically structured material ordered on both the meso scale and the atomic scale (Figure 1, black line).

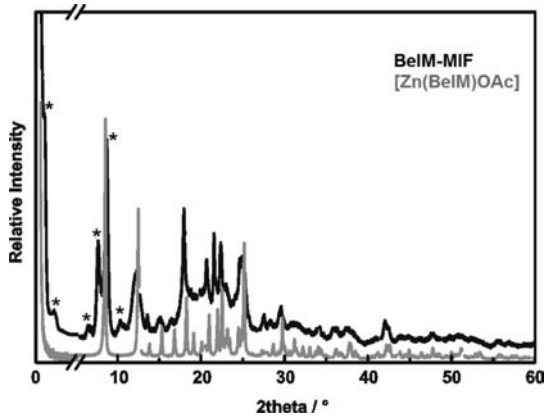

Figure 1. XRD powder patterns of mesostructured BeIM-MIF and the underlying 2D layered coordination polymer [Zn(BeIM)OAc]. 00*l* reflections of the lamellar mesostructure are marked with an asterisk. The patterns at low angles (0.5 to 5° 2θ) were measured in reflection mode, and at high angles (5 to 60° 2θ) in transmission mode.

Next, solid-state NMR and IR spectroscopy as well as mass spectrometry were used as local probes to elucidate the composition and bonding motifs in BeIM-MIF. The ^{13}C CP-MAS solid-state NMR spectrum of BeIM-MIF (Figure 2,

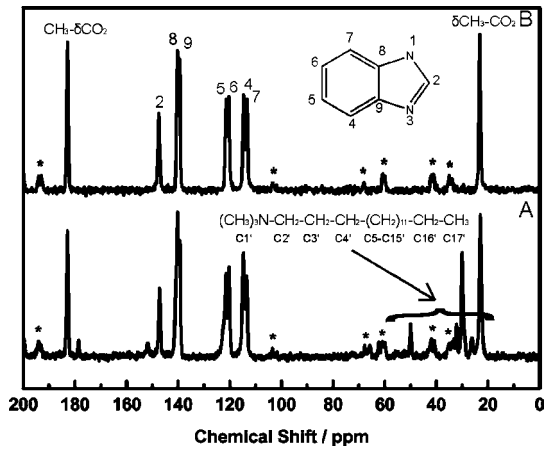

Figure 2. $^{13}C\{^1H\}$ MAS solid-state NMR spectra of (A) MIF-BeIM and (B) [Zn(BeIM)OAc]. Signals of the methylene chain partly overlap that of the methyl group of acetate. Signals marked with an asterisk are spinning side bands.

bottom) clearly indicates that both BeIM and CTAB are contained in the material; the presence of CTAB was also confirmed by mass spectrometry ($C_{19}H_{42}N^+$ peak at 284.6 *m*/*z*). On comparing the spectrum of BeIM-MIF with those of BeIM and CTAB, it is evident that the spectrum is not a mere overlay of the spectra of the starting materials. In BeIM-MIF, the ^{13}C positions next to N1/N3 (C8/C9 and C2) are shifted to lower field (139.5 ppm/140.3 ppm vs 134.9 ppm (pristine BeIM) for C8/C9 and 147.3 ppm vs 141.7 ppm (pristine BeIM) for C2) and the remaining benzene signals (C4/C7 at 114.7/113.6 ppm and C5/C6 at 121.5 ppm/120.4 ppm) are split. We therefore conclude that the chemical shifts and multiplet pattern of the ^{13}C signals are indicative of anionic [BeIM$^-$] as found in ZIF-7 ($Zn(BeIM)_2$) (see Table S1 in

dx.doi.org/10.1021/ja312567v | J. Am. Chem. Soc. 2013, 135, 6157−6164

Supporting Information [SI]), suggesting complete deprotonation of BeIM in contrast to proton-bearing BeIM(H).[44] The shifting and splitting pattern of the CTAB ^{13}C signals ranging from 55.1 to 14.3 ppm is similar to other mesostructured systems containing CTAB (Table S2 in SI).[37,45] Notably, the ^{13}C MAS solid-state NMR shows two additional peaks at 182.9 and 19.3 ppm, which originate from acetate anions (OAc), and a minor peak at 178 ppm suggesting the presence of a small amount of protonated HOAc moieties. For comparison, HOAc (in $CDCl_3$) has signals at 178.4 and 20.0 ppm[46] and solid $Zn(OAc)_2{\cdot}2H_2O$ at 183.7 and 19.3 ppm (Table S1 in SI), respectively. Obviously, by using zinc acetate as starting material OAc^- is incorporated into the system. What is more, OAc^- seems to play a crucial role for the formation of this compound as no precipitate was observed using alternative zinc sources such as $ZnCl_2$, $ZnBr_2$, ZnI_2, or $Zn(NO_3)_2$. While MeIM-MIF and IM-MIF are ternary systems Zn/(Me)IM/CTAB despite the presence of acetate ions in the microemulsion synthesis,[37] the ^{13}C NMR indicates that BeIM-MIF is in fact a quaternary system comprising Zn, BeIM, OAc, and CTAB.

IR measurements are in agreement with the above findings (Figure S1 in SI) and show the presence of small amounts of CTAB in BeIM-MIF through the two characteristic $\nu(CH_2)$-stretching vibrations at 2850 cm^{-1} and 2915 cm^{-1}.[37] Furthermore, characteristic BeIM and OAc ($\nu(C{=}O)$-stretching at 1542 cm^{-1}/1454 cm^{-1}) deformation and wagging modes are visible in the fingerprint region. In line with the NMR measurements, the absence of broad $\nu(OH)$ and $\nu(NH)$ stretching modes assignable to hydrogen-bonded proton-bearing acetic acid and benzimidazole above 1800 cm^{-1} points to fully deprotonated BeIM and OAc moieties.[46]

Basic Layered Structure. In order to shed light on the crystalline atomic-scale structure of the hybrid material as seen by high-angle XRD we carried out the synthesis under the same reaction conditions as stated above, yet with a gradually decreasing amount of CTAB, starting from 200 mL of a 0.05 M solution (= 100%) of CTAB in an *n*-heptane/1-hexanol/water microemulsion. Incorporation of CTAB starts at a CTAB content of 40% (200 mL of a 0.02 M solution) or higher, indicating the formation of micellar mesophases, which likely act as templates for the formation of the observed mesostructure. The XRD powder pattern of the product obtained without the addition of CTAB is depicted in Figure 1 (gray line). Clearly, the pattern no longer shows 00*l* reflections, indicating the absence of a mesostructure. The composition of the material was ascertained to correspond to the formula [Zn(BeIM)OAc] by elemental analysis (see below). Strikingly, most of the high-angle reflection positions and intensities are identical to those of BeIM-MIF, indicating the same underlying atomic ordering scheme in the mesostructured and the CTAB-free material. The close structural relationship between the two materials is confirmed by the ^{13}C solid-state NMR measurements, which exhibit the same chemical shifts and splitting patterns of the anionic building blocks [$BeIM^-$] and [OAc^-], and, hence, similar chemical environments (Figure 2). The XRD pattern of [Zn(BeIM)OAc] was indexed and refined by a Pawley fit ($P2_1/c$, a = 10.814 Å, b = 9.833 Å, c = 8.813 Å, β = 98.96°, Figure S2 in SI). The metrics match well with those of a known poly[μ_2-acetato−μ_2-benzimidazolato−zinc(cobalt)(II)] coordination polymer with composition [M(BeIM)OAc] (M = Co^{2+}/Zn^{2+}),[47,48] consisting of $M(BeIM)_{2/2}$ chains running along *b* and $M(OAc)_{2/2}$ chains running along *c*, which are connected by tetrahedrally coordinated M^{2+} ions, forming a 2D noninterpenetrated network (Figure 3a). In this layered hybrid framework, the 2D layers are oriented normal to the [100]-zone axis, connected by weak van der Waals interactions (Figure 3b). We therefore infer that the basic atomic-scale structure of BeIM-MIF is composed of [Zn(BeIM)OAc] layers, which are interleaved periodically by CTAB through liquid-crystal templating during the synthesis under reverse microemulsion conditions (see below).

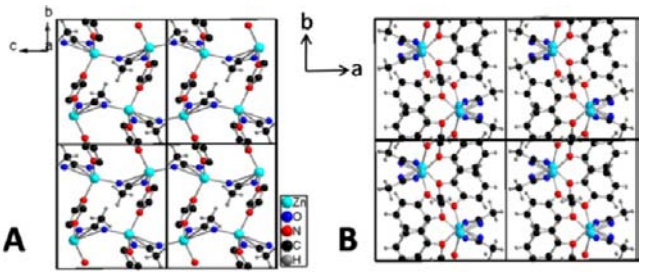

Figure 3. (A) Packing diagram of [Zn(BeIM)OAc] along the [100] axis highlighting the 2D sheets formed by $Zn(BeIM)_{2/2}$ chains and $Zn(OAc)_{2/2}$ chains connected by Zn^{2+} tetrahedra. The benzene rings of BeIM are omitted for clarity. (B) View along [001] showing the weak van der Waals interactions between different sheets.[47]

In line with these findings, elemental analysis (EA) of BeIM-MIF yields a [Zn^{2+}]:[$BeIM^-$]:[OAc^-]:[CTA^+Br^-] atomic ratio of roughly 7:7.5:6.5:1 (Table S4 in SI), whereas the composition of the CTAB-free material was determined as [Zn^{2+}]:[$BeIM^-$]:[OAc^-] = 1:1:1 (Table S5 in SI). The ligand-to-metal ratio is essentially the same for both compounds (∼1:1:1), and this is consistent with the previously observed high tendency of formation of hybrid compounds in the system Zn/(Be)IM/RCO_2.[47,49−51] The EA data of BeIM-MIF significantly differ from the data of the MIF systems Zn/MeIM/CTAB and Zn/IM/CTAB as the latter do not contain acetate ions but have a much higher CTAB content.[37] Also, the elemental composition of BeIM-MIF is distinct from that of the 3D zeolitic imidazolate frameworks (ZIFs), which show ratios of [Zn^{2+}]:[$BeIM^-$] of 1:2.[52]

Transmission Electron Microscopy. The above results suggest that layers of the coordination polymer [Zn(BeIM)-OAc] constitute the basic structural units, while the presence of CTAB gives rise to a superstructure with nanoscale periodicity, which modulates the atomically ordered, layered arrangement of [Zn(BeIM)OAc] along the stacking direction. To probe the interrelation between atomic-scale and mesoscale structure in BeIM-MIF we carried out chemical-composition line scans in the transmission electron microscope (TEM) using energy-dispersive X-ray spectroscopy (EDX) and electron energy-loss spectroscopy (EELS). Additionally, *Z*-contrast images using a high-angle annular dark-field (HAADF-STEM) detector were acquired. Measurements invariably reveal that the sample is extremely sensitive to the electron beam, thus requiring random selection of crystals and short acquisition times for the diffraction measurements, resulting in part in imperfect alignment of the sample with respect to the electron beam. TEM bright-field imaging adds evidence to the assumption of a lamellar mesostructure (Figure 4a). Although the morphology of the material resembles that of closely stacked and slightly spliced rods at first sight, a tilt series enabling us to view the assembly at three different angles confirms the presence of thin

dx.doi.org/10.1021/ja312567v | J. Am. Chem. Soc. 2013, 135, 6157−6164

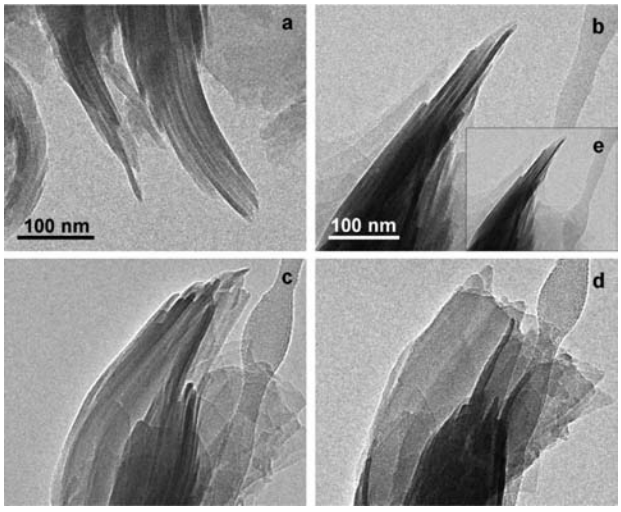

Figure 4. (a) Side view onto the lamellae; TEM tilt series (b–e) of BeIM-MIF showing the lamellar mesostructure. The images were obtained by rotating the TEM holder starting from (b) −25° to (c) 0°, to (d) +25° and (e) back to −25° (inset).

slabs stacked on top of each other (Figure.4b–d). Notably, the slabs have a tendency to roll up at their edges, thus conveying the impression of a curled or rodlike morphology.

The elemental distribution within the mesostructure was analyzed by EDX linescans for Zn and by EELS linescans for C and N, carried out on cross-section specimen of the material embedded in a polymer matrix (Figure 5). The TEM cross-

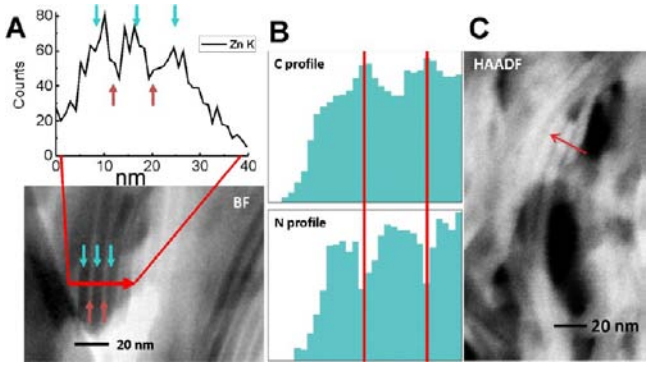

Figure 5. (A) EDX line scan of the Zn *K*-line intensity across BeIM-MIF layers in a polymer matrix. (B) EELS line scan across an HAADF image (C) of BeIM-MIF. The elemental distribution of Zn, N, and C was measured across several light and dark lamellae (spatial resolution ∼1 nm).

section image ascertains that the material is built up from lamellae featuring a periodic material contrast with a period of the dark and bright region of ∼8 nm. Notably, the elemental distribution profiles along the cross section indicate a higher amount of Zn in the dark regions (bright regions in the *Z*-contrast image indicating elements with higher *Z*), while the carbon content peaks in the smaller, bright regions (dark regions in the *Z*-contrast image indicating elements with smaller *Z*). A slightly higher nitrogen content in the dark regions may be inferred from the nitrogen distribution (Figure 5), thus suggesting that zinc and the nitrogen-containing ligand BeIM reside in the larger slabs, whereas the surfactant acts as a spacer. Hence, the Zn-containing dark slabs are composed of [Zn(BeIM)OAc] layers stacked along the [001] zone axis of the hybrid mesostructure, which are interleaved at regular intervals with a layer of CTAB, thus breaking up periodically the stacking of the [Zn(BeIM)OAc] layers of the pristine 2D structure as outlined in Scheme 1.

Scheme 1. Composite Mesostructure of BeIM-MIF, Composed of Layers of [Zn(BeIM)OAc] (in red) Stacked along [001], and Separated at Regular Intervals by CTAB (black)[a]

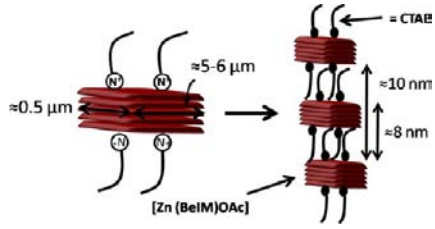

[a]Typical lateral dimensions of the anisotropic sheets are shown on the left; the basal spacing of ∼8 nm (10 nm for a stack covered by CTAB at the top and bottom) is indicated on the right.

This hypothesis is confirmed by selected-area electron diffraction (SAED) patterns collected along [001] of the mesostructure, giving rise to diffraction patterns of the (*hk*0) planes of the stacked lamellae. Indeed, simulations of the corresponding in-plane SAED patterns for pristine [Zn(BeIM)-OAc] (along [100] in the CTAB-free structure) compare well with those observed experimentally for the mesostructured material, thus confirming the atomic-level ordered structure of the lamellae, consistent with the composition and structure of [Zn(BeIM)OAc] (Figure 6).

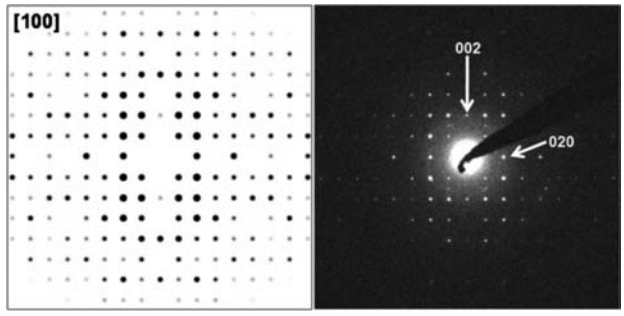

Figure 6. SAED pattern (right) of BeIM-MIF sonicated for 5 min in $CHCl_3$; simulation of the (0*kl*) plane (left) using the structure model of [Zn(BeIM)OAc].

Evidence of the mesostructure is obtained by SAED patterns taken parallel to the lamellae along [010] to probe the stacking period and shed light on the mutual arrangement of the Zn-hybrid layers and CTAB, respectively (Figure 7). The SAED pattern can be indexed on a series of 00*l* reflections, corresponding to a lattice spacing in the range of 80 ± 5 Å, which is consistent with the mesostructure seen by XRD (Figure 1). The modulated intensity distribution with strong 007 and weaker 006 and 008 reflections suggests the presence of a superstructure arising from a more subtle scattering contrast along the stacking direction. We associate the intensity modulation with the superposition of the layer stacking periodicity in the [Zn(BeIM)OAc] substructure (∼1.1 nm) with the mesostructure period of ∼8 nm, which results from the

dx.doi.org/10.1021/ja312567v | *J. Am. Chem. Soc.* 2013, 135, 6157–6164

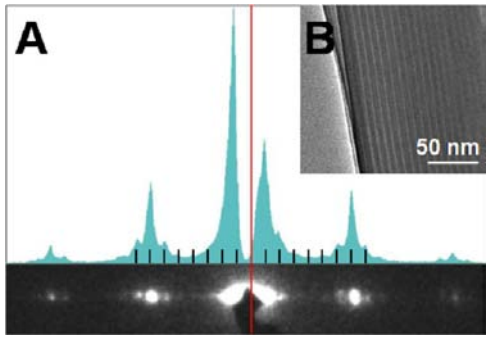

Figure 7. (A) SAED pattern and profile of BeIM-MIF viewed along [010] perpendicular to the corresponding lamellae (B) with a *d* value of ~82 Å.

ordered insertion of CTAB between the layers at regular intervals after roughly five to six layers of [Zn(BeIM)OAc]. In other words, the systematic disruption of the layer stacking sequence of the 2D layered coordination polymer by CTAB insertion gives rise to a regular mesostructure, where the modulated intensity distribution is reminiscent of the layer stacking period in the pristine acetato−benzimidazolato−zinc substructure.[53]

Surfactant Extraction. To confirm the above model and to examine the strength of interaction between the surfactant and hybrid layers within this stacked arrangement we carried out surfactant extraction experiments aiming at the complete removal of CTAB from the mesostructure, which should result in pure [Zn(BeIM)OAc]. Remarkably, the surfactant could only be removed by refluxing the material in EtOH or $CHCl_3$ for many hours, which was verified by ^{13}C solid-state NMR by monitoring the intensity of a characteristic CTAB signal at 55.1 ppm (representing the $-N(CH_3)_3^+$-group of CTAB) relative to the acetate peak of the hybrid layers at 182.9 ppm for increasing reflux times (Figures S6/S9 in SI). As outlined in Figure 8,

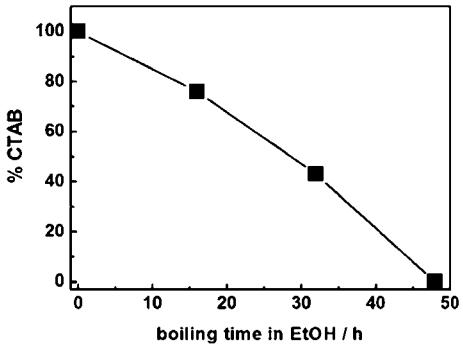

Figure 8. Time evolution of the extraction of CTAB from mesostructured MIF-BeIM. The CTAB content of the mesostructure is extracted from solid-state NMR measurements and plotted for increasing reflux times.

CTAB is gradually released during the course of several hours under reflux in EtOH, and is completely removed after 48 h, which is confirmed also by the XRD patterns of the extracted sample (Figure S5 and Table S6 in SI). On the one hand, this again highlights the close relationship between [Zn(BeIM)-OAc] and BeIM-MIF, as the latter is neatly transferrable into the former by surfactant extraction. On the other hand, the harsh conditions necessary to fully remove the surfactants indicate that strong interactions between the surfactants and the [Zn(BeIM)OAc] layers exist, which may even be an indication of grafting of the surfactants into the zinc-hybrid layers by direct bonding of Br^- to the neighboring [Zn(BeIM)-OAc] layer, while CTA^+ is electrostatically attached to the layers via CTA^+-Br^- interactions. The ^{15}N MAS NMR spectra of [Zn(BeIM)OAc] and BeIM-MIF (Figure S3 in SI) are largely in line with this hypothesis. The signal around −194.3 ppm can be assigned to the deprotonated nitrogen atoms N1/N3 of BeIM (−194.4 ppm for BeIM in [Zn(BeIM)OAc], −192.4 ppm for ZIF-7, whereas proton-bearing BeIM(H) has two signals at 145.2 and 223.5 ppm for N1/N3, respectively). The minor signal at −187.2 ppm may evidence slight charge redistribution at the BeIM nitrogen sites in the outer [Zn(BeIM)OAc] layers, which are in direct contact with CTAB, due to an increased Zn coordination sphere. However, the presence of impurity phases giving rise to this signal cannot be excluded. The quaternary nitrogen of CTAB is not visible in the ^{15}N NMR spectra, which in part may be due to the low concentration of CTAB compared to that of the hybrid layers but may also point to a significantly decreased mobility of the surfactant through grafting to the Zn-containing layers.

Exfoliation. The lamellar morphology of the mesostructure with its rolled up edges together with the structure model outlined above suggests that the lamellae are held together by van der Waals interactions between the hybrid material and the CTAB layers. Therefore, exfoliation of the multilayer stacks or even individual [Zn(BeIM)OAc] layers should be feasible by employing mechanical and solvent-assisted exfoliation protocols. To probe this hypothesis, exfoliation experiments of BeIM-MIF were carried out using different solvents, including ethanol (EtOH), dimethylformamide (DMF), water, chloroform ($CHCl_3$), toluene (Tol), and tetrahydrofuran (THF). The samples were shaken for 72 h until a milky colloidal suspension was obtained. The exfoliation efficiency decreases in the following order: THF > Tol > $CHCl_3$. Exfoliation in strongly polar solvents (i.e., water and DMF) was unsuccessful, as the solvent molecules apparently cannot efficiently penetrate between the hydrophobic interlayer space flanked by nonpolar benzene and methylgroups and filled by CTAB. The colloidal character of the suspensions obtained by exfoliation in THF, Tol, and $CHCl_3$ is evidenced by the Tyndall effect upon irradiation with a laser beam, with the finely dispersed nanosheets being the reason for scattering of the incident laser light (Figure 9).

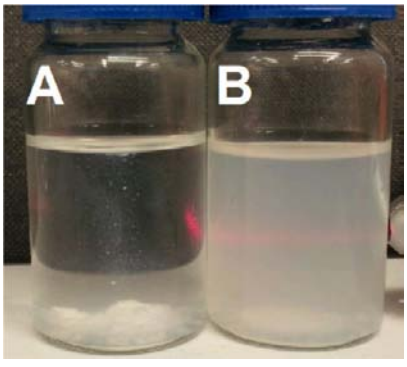

Figure 9. Demonstration of the Tyndall effect of a suspension of BeIM-MIF in toluene. While the red laser beam is invisible in the supernatant in (A) before exfoliation of BeIM-MIF, it is scattered by the colloidal suspension (B) containing BeIM-MIF nanosheets.

dx.doi.org/10.1021/ja312567v | *J. Am. Chem. Soc.* 2013, 135, 6157−6164

The colloidal suspensions were subsequently spin-coated on Si-wafers (~1.5 × 1.5 cm^2) for characterization by atomic force microscopy (AFM). Figure 10 shows typical AFM images of

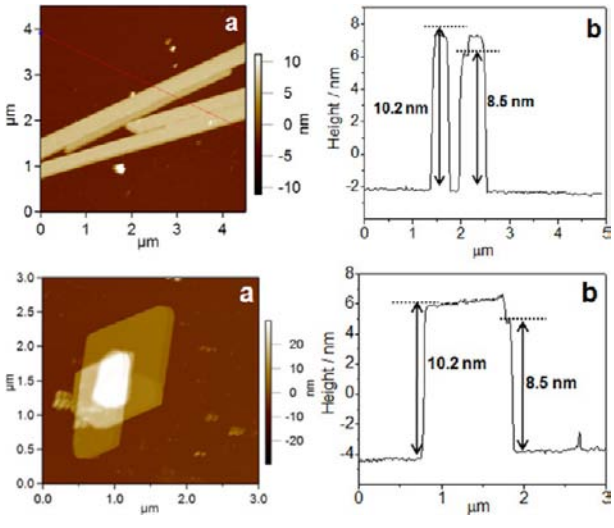

Figure 10. AFM surface topographies of BeIM-MIF exfoliated in different solvents. Top row: nanosheets exfoliated in Tol: (a) AFM image showing strongly anisotropic nanosheets (i.e., nanobelts/nanoribbons), (b) height profile. Bottom row: nanosheets exfoliated in THF: (a) AFM image, (b) height profile.

the morphology of BeIM-MIF after shaking in Tol and THF and subsequent spin-coating. The deposited particles display anisotropic lateral dimensions up to ~0.5 μm × ~5−6 μm (for Tol) with a beltlike morphology and a rhombohedral surface area of up 1.5 μm × 1.5 μm (for THF), respectively. Mainly anisotropic nanobelts were observed by AFM after exfoliation in Tol and THF, rather than sheets with equidistant lateral dimensions as seen via TEM on imaging the powdered sample without previous solution treatment. We attribute this fact to the mechanical disruption of the sheets during the shaking process, which reduces their lateral size and gives rise to the observed ribbon-shaped morphology. Notably, the measured heights for the deposited nanostructures are very uniform and amount to roughly 10.2 nm, which is consistent with the thickness of one dark and two bright lamellae, as determined by EDX/EELS measurements (Figure 5). Similarly, we observe a surface step of ~2 nm at the top of most nanobelts, which we tentatively attribute to a layer of CTAB as well as water covering the belts at the top and likely also at the bottom. To test whether the nanobelts can further be delaminated into smaller stacks of [Zn(BeIM)OAc] layers, the wafers showing ribbonlike nanostructures were immersed in an EtOH solution for 5 h. The resulting AFM images are shown in Figure S4 in SI. While the shape and lateral size of the nanostructures remains largely unchanged, the surface of BeIM-MIF roughens during the washing process. The measured heights after the washing step range from 4 to 7 nm, indicating that the nanobelts can in fact be reduced in height even further by ablating single [Zn(BeIM)OAc] layers from the top of the ribbon.

Nanotube Formation. A peculiar feature observed via TEM is the formation of nanotubular structures apart from extended sheets or belts (Figure 11D). SEM images reveal that these nanoscrolls are formed by self-rolling of one or more belts, similar to carbon nanoscrolls formed by the rolling up of

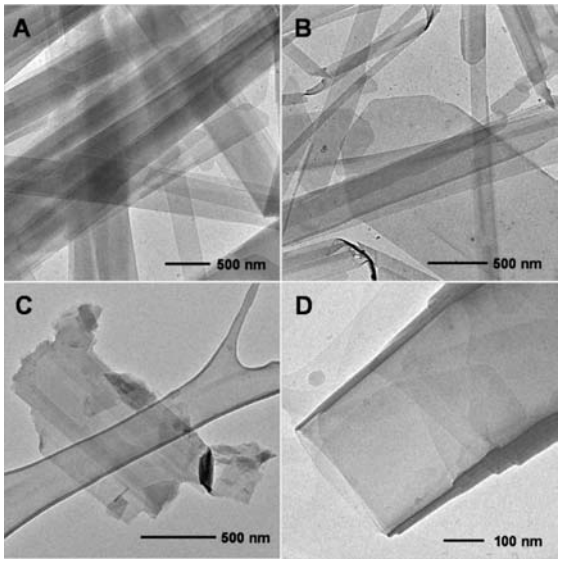

Figure 11. TEM images of BeIM-MIF exfoliated in THF. The material exhibits various nanomorphologies, including nanobelts (A), sheets, and intergrown belts (B and C), as well as multiwalled nanoscrolls (D).

graphene (Figure S10A in SI).[54,55] The nanoscrolls share the same in-plane structure and layered mesostructure as the nanosheets and belts, from which they seem to roll up into open, tubular structures with diameters ranging between 400 and 600 nm. This is consistent with the previously observed tendency of the sheets to buckle at their edges. Interestingly, the underlying periodicity of the lamellar mesostructure in the tubes is larger than that observed for the sheetlike lamellar mesostructure and amounts to roughly 10 nm. Note that nanotube formation is not a quantitative process and is only observed for samples which have been shaken in an organic solvent for exfoliation. We therefore infer that nanoscrolling occurs via a solution-mediated process, during which the CTAB layers are likely stripped off (Figure S10B vs S10A in SI). Together with charge inhomogeneities and surface strain induced by a loss of CTAB, this may lead to a higher tendency for spiral wrapping of the sheets to reduce the surface free energy through increased van der Waals forces. The formation of coordination polymer nanotubes next to extended sheet- and beltlike structures highlights the potential of this bottom-up synthesis for the creation of a diverse range of nanomorphologies, which can be tuned by varying the synthesis conditions.

Formation Mechanism. The coordination polymer mesostructure was only obtained under inverse microemulsion conditions in the presence of CTAB (>57 wt %), which points to the central role the surfactant plays in mesophase formation. The observed lamellar mesostructure featuring a precise pattern of hybrid inorganic slabs interleaved with organic slabs is in line with CTAB acting as a lamellar template, which is replicated by the spatially confined reaction of $Zn(OAc)_2$ and BeIM in the interlamellar space of the surfactant mesophase. The tentative formation mechanism is outlined in Scheme 2, highlighting the action of the CTAB mesophase as the confining template, which directs the gradual formation of the layered Zn-hybrid phase within the water reservoirs sandwiched between the organic liquid-crystal phase. This mechanism is in line with the observed hierarchical structure, which forms as a consequence

dx.doi.org/10.1021/ja312567v | J. Am. Chem. Soc. 2013, 135, 6157−6164

Scheme 2. Tentative Formation Mechanism of Mesostructured BeIM-MIF by Surfactant-Mediated Liquid-Crystal Templating under Reverse Microemulsion Conditions[a]

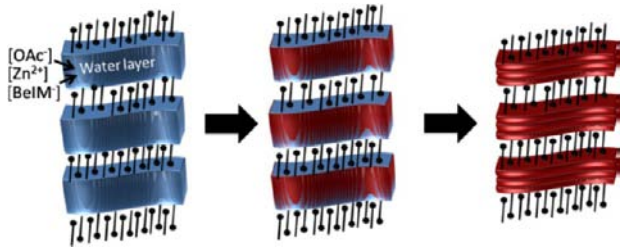

[a]CTAB forms a lamellar mesophase in the hydrophobic solvent, enclosing nanoscale water reservoirs (blue) as confined reaction space in which the coordination polymer nucleates. The consolidated structure (right) is composed of [Zn(BeIM)OAc] layers (red) interleaved with CTAB bilayers.

of both geometric confinement and interfacial free energy minimization at the organic−hybrid interface.

CONCLUSION

In summary, we have demonstrated the formation of a hierarchical coordination polymer mesostructure, which is obtained under reverse microemulsion conditions by surfactant mesophase templating. The lamellar mesostructure with a periodicity of 8 nm results from incorporation of CTAB into a crystalline layered [Zn(BeIM)OAc] structure at regular intervals, thus giving rise to stacks of nanosheets with a precisely defined number of layers, each stack being separated by CTAB. As opposed to the bonding situation in the mesostructured imidazolate frameworks reported previously (MIF-1 and MIF-2), the presence of acetate ions in BeIM-MIF apparently enables the formation of robust 2D nanosheets that form the underlying building blocks of the mesostructure reported in this work, thus giving rise to a material which is ordered on both the atomic scale and mesoscale. The stacks of nanosheets can be isolated by ultrasonic treatment, featuring a uniform size distribution of around 10 nm as determined by AFM under ambient conditions. Notably, we observe the formation of multiwalled nanotubular structures by rolling up of the 2D slabs owing to their highly flexible morphology, a phenomenon which has rarely been observed to date in the context of crystalline 2D coordination polymers.[8]

ASSOCIATED CONTENT

Supporting Information

Experimental details, IR spectroscopy, and ^{15}N solid state NMR spectroscopy measurements, elemental analysis of BeIM-MIF/[Zn(BeIM)OAc], Pawley fit of [Zn(BeIM)OAc], ^{13}C solid-state NMR/XRD/TEM measurements on different solvent extracted samples. This material is available free of charge via the Internet at http://pubs.acs.org.

AUTHOR INFORMATION

Corresponding Author

b.lotsch@fkf.mpg.de

Notes

The authors declare no competing financial interest.

ACKNOWLEDGMENTS

Financial support by the Max-Planck Society, Nanosystems Initiative Munich (NIM), Center for Nanoscience (CeNS), and Fonds der Chemischen Industrie (FCI) is gratefully acknowledged. We thank C. Minke and Dr. J. Weber for solid-state NMR measurements, H. Hartl and M.-L. Schreiber for ICP measurements, and Dr. M. Konuma for XPS-measurements. We are indebted to Prof. L. Kienle for helpful discussions on the TEM analysis and C. Donadel for practical support. We are grateful to Prof. P. Van Aken (MPI-IS, Stuttgart), head of the StEM group, for granting access to the TEM facility. We thank B. Bussmann for TEM cross-section preparation (MPI-IS, Stuttgart).

REFERENCES

(1) Alivisatos, A. P. *Science* **1996**, *271*, 933−937.
(2) Thakur, P. Y.; Ram, M. Y.; Dinesh, P. S. *Nanosci. Nanotechnol.* **2012**, *2*, 22−48.
(3) Adachi, M.; Nakagawa, K.; Sago, K.; Murata, Y.; Nishikawa, Y. *Chem. Commun.* **2005**, 2381−2383.
(4) Nakagawa, K.; Yamaguchi, K.; Yamada, K.; Sotowa, K.-I.; Sugiyama, S.; Adachi, M. *Eur. J. Inorg. Chem.* **2012**, , 2741−2748.
(5) Xu, C.; Zeng, Y.; Rui, X.; Xiao, N.; Zhu, J.; Zhang, W.; Chen, J.; Liu, W.; Tan, H.; Hng, H. H.; Yan, Q. *ACS Nano* **2012**, *6*, 4713−4721.
(6) Pham, M.-H.; Vuong, G.-T.; Fontaine, F.-G.; Do, T.-O. *Cryst. Growth Des.* **2012**, *12*, 3091−3095.
(7) Kijima, T.; Nagatomo, Y.; Takemoto, H.; Uota, M.; Fujikawa, D.; Sekiya, Y.; Kishishita, T.; Shimoda, M.; Yoshimura, T.; Kawasaki, H.; Sakai, G. *Adv. Funct. Mater* **2009**, *19*, 545−553.
(8) Jang, J.-t.; Jeong, S.; Seo, J.-w.; Kim, M.-C.; Sim, E.; Oh, Y.; Nam, S.; Park, B.; Cheon, J. *J. Am. Chem. Soc.* **2011**, *133*, 7636−7639.
(9) Vaughn, D. D., II; Patel, R. J.; Hickner, M. A.; Schaak, R. E. *J. Am. Chem. Soc.* **2010**, *132*, 15170−15172.
(10) Waller, M. R.; Townsend, T. K.; Zhao, J.; Sabio, E. M.; Chamousis, R. L.; Browning, N. D.; Osterloh, F. E. *Chem. Mater.* **2012**, *24*, 698−704.
(11) Gao, M.-R.; Yao, W.-T.; Yao, H.-B.; Yu, S.-H. *J. Am. Chem. Soc.* **2009**, *131*, 7486−7487.
(12) Centi, G.; Perathoner, S. *Microporous Mesoporous Mater.* **2008**, *107*, 3−15.
(13) Manos, M. J.; Petkov, V. G.; Kanatzidis, M. G. *Adv. Funct. Mater* **2009**, *19*, 1087−1092.
(14) Lee, K. K.; Loh, P. Y.; Sow, C. H.; Chin, W. S. *Biosens. Bioelectron.* **2013**, *39*, 255−260.
(15) Gérardin, C.; Kostadinova, D.; Sanson, N.; Coq, B.; Tichit, D. *Chem. Mater.* **2005**, *17*, 6473−6478.
(16) Geng, F.; Xin, H.; Matsushita, Y.; Ma, R.; Tanaka, M.; Izumi, F.; Iyi, N.; Sasaki, T. *Chem.—Eur. J.* **2008**, *14*, 9255−9260.
(17) Yuan, C.; Li, J.; Hou, L.; Zhang, X.; Shen, L.; Lou, X. W. *Adv. Funct. Mater* **2012**, *22*, 4592−4597.
(18) Na, K.; Jo, C.; Kim, J.; Cho, K.; Jung, J.; Seo, Y.; Messinger, R. J.; Chmelka, B. F.; Ryoo, R. *Science* **2011**, *333*, 328−332.
(19) Patil, A. J.; Mann, S. *J. Mater. Chem.* **2008**, *18*, 4605−4615.
(20) Miyamoto, N.; Kuroda, K.; Ogawa, M. *J. Mater. Chem.* **2004**, *14*, 165−170.
(21) Ida, S.; Ogata, C.; Eguchi, M.; Youngblood, W. J.; Mallouk, T. E.; Matsumoto, Y. *J. Am. Chem. Soc.* **2008**, *130*, 7052−7059.
(22) Ramakrishna Matte, H. S. S.; Gomathi, A.; Manna, A. K.; Late, D. J.; Datta, R.; Pati, S. K.; Rao, C. N. R. *Angew. Chem., Int. Ed.* **2010**, *49*, 4059−4062.
(23) Omomo, Y.; Sasaki, T.; Wang; Watanabe, M. *J. Am. Chem. Soc.* **2003**, *125*, 3568−3575.
(24) Ma, R.; Takada, K.; Fukuda, K.; Iyi, N.; Bando, Y.; Sasaki, T. *Angew. Chem., Int. Ed.* **2008**, *47*, 86−89.
(25) Keller, S. W.; Kim, H.-N.; Mallouk, T. E. *J. Am. Chem. Soc.* **1994**, *116*, 8817−8818.

(26) Li, P.-Z.; Maeda, Y.; Xu, Q. *Chem. Commun.* **2011**, *47*, 8436−8438.
(27) Amo-Ochoa, P.; Welte, L.; Gonzalez-Prieto, R.; Sanz Miguel, P. J.; Gomez-Garcia, C. J.; Mateo-Marti, E.; Delgado, S.; Gomez-Herrero, J.; Zamora, F. *Chem. Commun.* **2010**, *46*, 3262−3264.
(28) Li, Z.-Q.; Qiu, L.-G.; Wang, W.; Xu, T.; Wu, Y.; Jiang, X. *Inorg. Chem. Commun.* **2008**, *11*, 1375−1377.
(29) Yuan, Y.; Wang, W.; Qiu, L.; Peng, F.; Jiang, X.; Xie, A.; Shen, Y.; Tian, X.; Zhang, L. *Mater. Chem. Phys.* **2011**, *131*, 358−361.
(30) Tan, J. C.; Cheetham, A. K. *Chem. Soc. Rev.* **2011**, *40*, 1059−1080.
(31) Saines, P. J.; Jain, P.; Cheetham, A. K. *Chem. Sci.* **2011**, *2*, 1929−1939.
(32) Li, W.; Barton, P. T.; Burwood, R. P.; Cheetham, A. K. *Dalton Trans.* **2011**, *40*, 7147−7152.
(33) Tan, J.-C.; Jain, P.; Cheetham, A. K. *Dalton Trans.* **2012**, *41*, 3949−3952.
(34) Saines, P. J.; Barton, P. T.; Jain, P.; Cheetham, A. K. *Cryst. Eng. Commun.* **2012**, *14*, 2711−2720.
(35) Saines, P. J.; Tan, J.-C.; Yeung, H. H. M.; Barton, P. T.; Cheetham, A. K. *Dalton Trans.* **2012**, *41*, 8585−8593.
(36) Tan, J.-C.; Saines, P. J.; Bithell, E. G.; Cheetham, A. K. *ACS Nano* **2011**, *6*, 615−621.
(37) Junggeburth, S. C.; Schwinghammer, K.; Virdi, K. S.; Scheu, C.; Lotsch, B. V. *Chem.—Eur. J.* **2012**, *18*, 2143−2152.
(38) Huo, Q.; Margolese, D. I.; Ciesla, U.; Demuth, D. G.; Feng, P.; Gier, T. E.; Sieger, P.; Firouzi, A.; Chmelka, B. F.; Schüth, F.; Stucky, G. D. *Chem. Mater.* **1994**, *6*, 1176−1191.
(39) Wang, Y.; Sun, X.; Li, H. *Mater. Sci. Eng. B* **2010**, *167*, 177−181.
(40) Z. Khimyak, Y.; Klinowski, J. *J. Chem. Soc., Faraday Trans.* **1998**, *94*, 2241−2247.
(41) Chen, L.; Klar, P. J.; Heimbrodt, W.; Oberender, N.; Kempe, D.; Fröba, M. *Appl. Phys. Lett.* **2000**, *77*, 3965−3967.
(42) Martin, J. D.; Keary, C. L.; Thornton, T. A.; Novotnak, M. P.; Knutson, J. W.; Folmer, J. C. W. *Nat. Mater.* **2006**, *5*, 271−275.
(43) Sun, Y.; Afanasiev, P.; Vrinat, M.; Coudurier, G. *J. Mater. Chem.* **2000**, 2320−2324.
(44) Grant, D. M.; Pugmire, R. J. *J. Am. Chem. Soc.* **1971**, *93*, 1880−1887.
(45) Khimyak, Y. Z.; Klinowski, J. *Phys. Chem. Chem. Phys.* **2001**, *3*, 616−626.
(46) Hesse, M.; Meier, H.; Zeeh, B., *Spektroskopische Methoden in der Organischen Chemie*; Thieme: Stuttgart, 2005; Vol. 7.
(47) Li, X.-M. *Acta Crystallogr., Sect. E* **2007**, *63*, m1984.
(48) Arai, L.; Nadeem, M. A.; Bhadbhade, M.; Stride, J. A. *Dalton Trans.* **2010**, *39*, 3372−3374.
(49) Chen, S.-S.; Chen, Z.-H.; Fan, J.; Okamura, T.-a.; Bai, Z.-S.; Lv, M.-F.; Sun, W.-Y. *Cryst. Growth Des.* **2012**, *12*, 2315−2326.
(50) Weitzel, G.; Fritzdorff, A.-M. *Chem. Ber.* **1956**, *Bd. 305*, 1−19.
(51) Martins, G. A. V.; Byrne, P. J.; Allan, P.; Teat, S. J.; Slawin, A. M. Z.; Li, Y.; Morris, R. E. *Dalton Trans.* **2010**, *39*, 1758−1762.
(52) Park, K. S.; Ni, Z.; Côte, A. P.; Choi, J. Y.; Huang, R.; Uribe-Romo, F. J.; Chae, H. K.; O'Keeffe, M.; Yaghi, O. M. *Proc. Natl. Acad. Sci. U.S.A.* **2006**, *103*, 10186−10191.
(53) Schürmann, U.; Duppel, V.; Buller, S.; Bensch, W.; Kienle, L. *Cryst. Res. Technol.* **2011**, *46*, 561−568.
(54) Viculis, L. M.; Mack, J. J.; Kaner, R. B. *Science* **2003**, *299*, 1361.
(55) Braga, S. F.; Coluci, V. R.; Legoas, S. B.; Giro, R.; Galvão, D. S.; Baughman, R. H. *Nano Lett.* **2004**, *4*, 881−884.